Future volcanic eruptions shift the timing of net-zero emissions

Moritz Adam[1,2,*], Tom Schürmann[1], Kira Rehfeld[1,2,3],

1 Department of Geosciences, University of Tübingen, Tübingen, Germany
2 Cluster of Excellence (EXC 3121): TERRA – Terrestrial Geo-Biosphere Interactions in a Changing World, University of Tübingen, Tübingen, Germany
3 Department of Physics, University of Tübingen, Tübingen, Germany

* moritz.adam@uni-tuebingen.de

Abstract

Volcanic eruptions are inevitable, unpredictable, and impact climate globally. During outbreaks, volcanic aerosols enter the stratosphere, modifying the planetary energy balance. How eruptions affect biosphere carbon uptake is unclear, as including the possible forcing trajectories in climate model projections is computationally expensive. Here, we show realistic future volcanic forcing increases projected regional temperature variability for the overshoot scenario SSP5-3.5-OS and adds uncertainty to biosphere carbon sink capacity estimates. We use intermittent eruption trajectories to derive 300 estimates of future climate and biosphere productivity from a computationally efficient, regionally explicit simulator. Global mean temperature pathway uncertainty relative to the internal component is, on average, 0.32 °C (+89 %) larger with intermittent forcing. Propagating this uncertainty into net carbon uptake through shared variances between climatic drivers and the biosphere's response increases regional uncertainty by up to 34 % of internal variability. Regionally, uncertainty in annual temperature is increased by 50 %+ for half of the world's population. Effects aggregate globally, potentially delaying or advancing net-zero emissions and planetary temperature stabilization.

Introduction

Intermittent external forcing of the climate system arises from stratospheric aerosol emissions from largely unpredictable volcanic eruptions. These varying perturbations significantly increase global temperature variability and future projection uncertainty [1, 2]. Due to computational constraints, regional assessments are not yet widely considered. Climate records indicate that regional climate variability may increase under future volcanic forcing [3]. Higher regional variability in surface air temperature and hydroclimate may increase weather extremes, which challenges biosphere carbon sink resilience and local climate change adaptation and mitigation measures. Volcanic perturbations may amplify modes of variability like ENSO [4] and blur warming or stabilization trend attribution [2]. We develop a strategy for resolving regional uncertainties along future projection pathways until 2200 (Data and methods), and apply a large paleo-informed forcing dataset as an analogue for "realistic" future volcanic forcing [5]. Our ensemble median forcing (Data and methods) matches the constant mean forcing suggested for CMIP7 simulations [2, 6].

Life on land needs light and water, which means intermittent volcanic forcing with changes in surface (hydro-)climate can impact terrestrial and marine carbon fluxes.

Considering this could yield more representative uncertainty estimates for the efficiency of future carbon sinks and sources. However, the magnitude of future carbon cycle responses to sporadic eruptions remains unquantified. Terrestrial and marine carbon reservoirs currently buffer anthropogenic CO_2 emissions but re-equilibrate under future climate change [7]. In likely [8] temperature overshoot scenarios, such re-equilibration dynamics are expected to be particularly strong [9]. Whether intermittent volcanic forcing stimulates or reduces natural carbon uptake under future warming, or does both, is unclear. The associated cooling and surface radiation reduction could affect various processes across Earth system compartments connected to carbon uptake. Cooling enhances the marine CO_2 solubility pump and secondary effects could influence the ocean's biological pump [10]. On land, intermittent aerosol forcing causes slight solar dimming and can alter climate, including precipitation patterns and evapotranspiration feedbacks. These influence plant water-use efficiency, moisture availability for vegetation, and carbon-positive organic matter decomposition in soils [11–13]. Missing these supplementary uncertainty sources for the carbon sinks impacts future emission budget accuracy.

If sporadic volcanic eruptions are represented in IPCC-class Earth system model (ESM) simulations, this is usually achieved by varying aerosol optical depth of the upper atmosphere (AOD). However, realistic intermittency is not considered in projections following shared socioeconomic pathways (SSPs) [14]. Future eruption timings and magnitudes are unknown, so stable uncertainty estimates require ensemble simulations [1]. This is computationally costly and intractable with ESM simulations for multiple scenarios or model intercomparison. Several statistical approaches have explored emulating future global-mean responses of ESMs to intermittent volcanic forcing [2] or replicating historical temperature evolution [15, 16]. This leaves open challenges of using, for example, linear pattern scaling or machine learning for spatially explicit emulation in order to then generate larger ensembles than those possible with ESM simulations [16].

Our emulation approach balances being physically grounded and tractable, and suitability for broader problems, including low data availability, internal variability and non-linearities [17]. From a certain magnitude, volcanic eruptions trigger distinct forced responses of climate modes. Therefore, we address the challenge of a sufficiently large simulation ensemble by combining semi-stochastically forced simulations from the comprehensive MPI-ESM [18] with a statistical emulator of the model's forced response modes (Data and methods). Our Bayesian approach estimates parameters of a stochastic two-box energy balance model (EBM), representing forced and internal variability components. This EBM approach generalizes from Schillinger et al. (2022) [15] to fit two response timescales and two thermodynamic inertias per dominant spatial mode of variability. This enables emulation of spatially resolved, globally consistent temperature time series (Data and methods).

The emulator lets us study spatially resolved Earth system effects of realistic volcanic eruptions under future climate change. We derive an ensemble of 300 forcing realizations along the extended SSP5-3.4-OS temperature overshoot scenario until 2200 [14, 19]. This quantifies supplementary variability in global and regional surface climate from intermittent volcanic forcing (Fig. 1a, b). Based on temperature and moisture variance estimates, we infer supplementary uncertainty in vegetation productivity and carbon uptake into land and ocean sinks regionally and globally, which has the potential to affect the timing of net-zero emissions and temperature stabilization.

Data and methods

We combine Earth system model simulations driven by realistic, intermittent volcanic eruptions with an emulator based on a stochastic EBM, which operates on the dominant spatiotemporal modes of temperature variability. Using the covariance between climatic drivers and biotic response variables, we leverage the emulator to estimate the supplementary uncertainty that volcanic variability induces on surface climate and carbon fluxes. The variability assessment utilizes power spectra and variance ratios.

Earth system model simulations of a temperature overshoot scenario with intermittent, paleo-informed volcanic forcing

Simulations with the Max–Planck–Institute Earth system model (MPI-ESM) version 1.2 [18] provide the basis for our study. They serve to quantify the Earth system response to intermittent volcanic forcing in general (S1 Text), emulate the simulated surface climate's forced response (next section), and estimate the covariance between climatic and biotic variables. We operate the ECHAM6.3 atmosphere model [20] with a T63 spectral truncation (approximately 200 km grid spacing) and the MPIOM ocean model [21] on a GR15 grid (150 km approximate spacing). The model setup features a fully coupled, nitrogen-limited terrestrial and marine carbon cycle, run in an emission-driven mode. Boundary conditions for greenhouse gases and land use follow the CMIP6 and ScenarioMIP protocols [22] and their long-term extensions [19]. ECHAM6.3 parametrizes the radiative impact of external volcanic forcing as modulations of aerosol optical depth (AOD).

We leverage the PalVolv1 dataset of past volcanic eruptions [5] as a paleo-informed boundary condition to model future intermittent volcanic forcing. PalVolv1 is a unique resource that combines the paleo-record of eruptions from the last 130.000 years with stochastic sampling of smaller-sized eruptions. PalVolv1 corrects for the typical undersampling of small volcanic eruptions by augmenting the paleo-record with stochastically sampled small events which results in a more realistic distribution of occurrences. Out of the 100 realizations in the PalVolv1 dataset, we selected the 50^{th} member for our study. To convert PalVolv1 into forcing realizations for our MPI-ESM simulations, we first subdivide the median realization into five non-overlapping 185-year time segments. These selected segments are spaced apart by at least 1000 years. Subsequently, three of the segments are shifted forward in time by 61 years, increasing the ensemble size to eight members. This approach reduces biases in the distribution of events over time, albeit not eliminating them entirely (S7 Fig). This yields more reliable mean climatologies (S1 Text) and has no impact on the emulator's parameter estimates (next section, S4 Fig). In contrast to the volcanic forcing of varying intensity, each member of the climatological control ensemble experiences the median event of one of the stochastically forced simulations. This yields an ensemble of background climatologies without the timely varying volcanic influence on climate variability.

Our goal with the emulator is to derive a time-stable and more realistic uncertainty envelope for SSP storylines. We therefore divide the selected PalVolv1 realization into time series segments of 185 years. We cut 300 members out of the time frame 79.000–23.500 before present. Each of these are then fed into the Easy Volcanic Aerosol (EVA) forcing generator [23]. EVA employs a three-box parametrization of aerosol transport in the stratosphere and a simple scaling relationship between aerosol mass and AOD to convert aerosol load, timing, and location of volcanic eruptions into aerosol optical properties by latitude and radiative band [23]. The ensemble median stratospheric AOD at 550 nm is 0.014, closely matching the constant mean AOD value assumed for 2015–2100 in CMIP7 [6] and the median of the stochastic forcing ensemble used by Chim et al. (2025) [2] to drive their global impulse–response function approach.

Separating internal climate variability and forced response of the simulated surface air temperature

We expand the two-box emulator approach of Schillinger et al. (2022) [15] to spatiotemporal data. For this purpose, we decompose the simulated temperature data into empirical orthogonal functions (EOFs, S2 Fig) and fit a stochastic EBM to the resulting principal components of variability. EOFs are a standard approach for reducing the dimensionality of spatiotemporal data [24]. Essentially, the EOF method uses spatiotemporal covariance in the data to perform a base decomposition into dominant and orthogonal spatial modes. Each mode is associated with a time series ("principal component") representing the variations of that mode. For our study, we perform a decomposition into ten spatial modes and principal components using the entire annually averaged surface air temperature dataset from MPI-ESM simulations with intermittent aerosol forcing from 2015 to 2200 (S1 Fig). These ten orthogonal modes capture 69 % of the variability contained in the data. The first seven modes already account for 66 % of the overall variance. This truncation results in a root mean square error (RMSE) of 0.3 K averaged over space and time. After the spatial decomposition we linearly regress relevant principal component time series onto the CO_2-forcing and subtract CO_2 trends from principal component time series (S1 Fig).

Finally, we fit the two-box EBM on each principal component to separate the forced response to external volcanic forcing from internal variability (S1 Fig, S3 Fig). For this step, we employ the ClimBayes package [15], with prior ranges and parameters of the fitting algorithm as documented in S1 Table and the original publication. The stochastic model resolves space implicitly through the upstream EOF decomposition. Therefore, as input for the EBM, we globally average the latitudinally resolved ESM forcing and limit it to the 550 nm band (441.5–625 nm). We conduct the Bayesian inference step [15] separately for each forcing realization, yielding an ensemble of EBM parameters for each principal component (S4 Fig). These parameters describe the dynamics of the principal components and are consequently dimensionless. However, they still provide insights into the characteristic physical timescales and (thermo-)dynamic inertia of the spatial modes (S4 Fig). In addition, comparing the parameters between different realizations confirms that the EBM fitting is stable across them (S4 Fig), justifying using the median value of each EBM parameter for projections.

We exploit the fitted EBM in two ways. The first separates the internal and forced components of surface air temperature fields by recombining the EOFs with either the forced or internal contributions to the principal components. Core to the stochastic EBM, this assumes additivity of the forced and internal variability components. The second turns the fitted EBM into an emulator of the MPI-ESM forced response to intermittent volcanic forcing by inverting it with new forcing realizations and recombining the spatiotemporal decomposition (S1 Figb). Since we focus on the effects of volcanic forcing in both cases and not those of CO_2, we report the internal variability component with the longer-term CO_2 trend included, even though CO_2 emissions are also an external forcing. This design choice ensures that all variability components presented in the figures add up to the original variability. The average RMSE is 0.019 K between the inverted EBM and the recombined EOF truncation, and 0.027 K when comparing the ten-year mean response after the 30 % strongest volcanic events between the fit and the ESM simulations.

We define the uncertainty $q(t)$ of regional and global future projections as the 95 % inter-quartile range of a simulation ensemble at time t with inter-quartile range q_j

$$q_j = q_{u-l}(t) = q_u(t) - q_l(t)$$

and the specific case

$$q(t) \coloneqq q_{97.5-2.5}(t) = q_{97.5}(t) - q_{2.5}(t)$$

where the lower and upper linear empirical sample quantiles q_l and q_u are set to the 2.5^{th} and 97.5^{th} quantile, respectively. In our convention, this uncertainty envelope encompasses both the forced and internal variability components. We denote the uncertainty envelope q^{int} if the forced response has been excluded.

Estimating the additional uncertainty of regional and global carbon fluxes and their climatic drivers due to volcanic forcing

We provide a first-order estimate of the supplementary uncertainty that intermittent volcanic forcing adds to natural carbon fluxes at regional and global levels. To achieve this, we propagate the uncertainty increase relative to internal variability – which was determined explicitly for surface air temperature – by weighting it according to the shared variance between carbon fluxes and climatic drivers. Here, we assume surface air temperature (T) and the hydrological cycle are the predominant drivers of (terrestrial) vegetation productivity (f_{GPP}) and (terrestrial+marine) net CO_2 uptake into natural sinks (f_{nat}). We consider either precipitation (P) or soil moisture (M) as proxies for hydrological conditions. The shared variance between observables i, j is defined by the Pearson correlation ρ.

$$r_{i\times j} = \rho\left(x_i, x_j\right)^2$$

For the regional analysis, we determine shared variances $r_{i\times j}$ for each region using annually averaged data. On the global scale, a variable windowing takes place when necessary (next section).

Based on the ratio between forced+internal and internal temperature uncertainty, and assuming the shared variance does not change substantially over the time interval of interest, the relative change $\Delta^r q_i = {}^{q_i}/_{q_i^{int}} - 1$ in precipitation uncertainty is

$$\Delta^r q_P = \Delta^r q_T \cdot r_{T\times P}$$

The computation for soil moisture as the hydrological proxy is analogous. For the carbon fluxes, illustrated for f_{GPP} below, we assume that temperature and hydroclimate contribute additively without overlapping.

$$\begin{aligned}\Delta^r q_{f_{GPP}} &= \Delta^r q_T \cdot r_{T\times f_{GPP}} + \Delta^r q_P \cdot r_{P\times f_{GPP}} \\ &= \Delta^r q_T \cdot \left(r_{T\times f_{GPP}} + r_{T\times P} \cdot r_{P\times f_{GPP}}\right)\end{aligned}$$

This simplification is adequate for a first-order estimate since typically either temperature or moisture exerts dominant control over regional vegetation productivity, but not both simultaneously. The correlation between precipitation and the ocean–atmosphere carbon flux is negligible in the first place. We compare uncertainty changes to the total annual carbon fluxes $\left[f_{GPP}\right]$, $\left[f_{nat}\right]$ by rescaling the relative uncertainty change with respect to internal variability using the ratio between internal variability and total fluxes.

$$\Delta^r q_{f_{GPP}} \cdot \frac{q^{int}_{f_{GPP}}}{\left[f_{GPP}\right]} = \frac{q_{f_{GPP}} - q^{int}_{f_{GPP}}}{\left[f_{GPP}\right]}$$

Estimates of increased SSP uncertainty

Deriving global uncertainty cones along the SSP pathway relies on the same reasoning. However, instead of scaling only uncertainties defined by inter-quartile ranges, we

perform an empirical quartile transformation of the MPI-ESM grand ensemble's [25] unforced uncertainty distributions. This extension accounts for asymmetries in the distributions when propagating increased uncertainty through additional variability components. As a first step, we diagnose the relative difference in each inter-quartile range q^j between T in our emulated ensemble with intermittent volcanic forcing and T in our control ensemble (index j subsequently dropped for readability). As before, the propagated uncertainty increase δq_i for the first- and second-order response variables ($i \in \{P, M, f_{GPP}, f_{nat}\}$) results from their shared variances (index i subsequently dropped).

$$\delta q = \Delta^r q \cdot q^{int}$$

Next, for each of those variables, we calibrate the quartile transformation based on simulations with intermittent forcing and the control ensemble using a weighting factor a_u

$$a_u = \frac{q_u^v - m^v}{m^v - q_l^v} \cdot \frac{m^c - q_l^c}{q_u^c - m^c}$$

where m^v, m^c are the medians of the volcano-forced and the control case, respectively. a_u captures the contributions of a shifting upper quartile q_u and lower quartile q_l to the change in inter-quartile range δq. The contribution of q_u is given by

$$\tilde{a}_u^j = \frac{a_u^j}{1 + a_u^j}$$

and of q_l by

$$\tilde{a}_l^j = \frac{1}{1 + a_u^j}$$

Then, the transformed quartiles are given by

$$q_u = q_u^c + \delta q \cdot \tilde{a}_u$$
$$q_l = q_l^c - \delta q \cdot \tilde{a}_l$$

S13 Fig displays the resulting distributions for different timescales. These uncertainty estimates are rather conservative, since we calibrate the quartile transformation on the relationship between simulations with intermittent volcanic forcing and median event forcing (control), but apply it to the MPI-ESM grand ensemble [25], which does not include varying volcanic forcing (also no median event). While sub-decadal variability dominates the overall uncertainty distributions, varying volcanic forcing stimulates multi-annual to multi-decadal climate in particular, which is reflected in overproportionally high relative uncertainty increase on these time scales (S13 Fig).

Computing power spectra and variance ratios

Power spectra provide insight into the relative importance of variations on specific timescales for the overall variability of a variable. Mathematically, the power spectral density (PSD) is the Fourier transform of a time series' autocovariance function. To minimize artefacts when computing power spectra, the multitaper approach has proven reliable and superior to non-parametric approaches. Here, we employ it in the same way as Ellerhoff et al. (2021) [26] to compute the PSD with corresponding uncertainties. Similar to Schillinger et al. (2022) [15], the PSD is smoothed logarithmically with a Gaussian kernel of 0.04 dB. To obtain timescale dependent variance ratios, we divide the PSD estimate of interest by that of the baseline experiment and propagate the uncertainties based on the PSD's degrees of freedom following Ellerhoff et al. (2021) [26].

Computation of the relative global variance increase $\hat{\sigma}^2$ differs by variable. For the global mean surface air temperature, we infer it directly from the variance ratio of forced realizations to the model's internal variability

$$\hat{\sigma}^2(\tau) = \frac{\sigma^2_{\text{forced}}}{\sigma^2_{\text{internal}}}(\tau) - 1$$

Increases in variance of the remaining variables build on propagating this temperature uncertainty on logarithmically spaced time intervals with the shared variance approach. For this purpose, we first apply a Gaussian bandpass filter to the global time series for each time interval and compute the shared variance. We use these time-scale-dependent values to compute the scaling factors described in the previous section.

Results

Increased multi-annual to -decadal climate and biosphere variability along the temperature overshoot

We investigate intermittent aerosol forcing's potential to shift the timing of net-zero emissions along an overshoot pathway (Fig. 1a). Our simulations show volcanic aerosols reduce energy input over most land and many ocean regions (S7 Figc), causing almost universal cooling, particularly over land and in mid- to high-latitudes (S7 Fig, S1 Text). A belt from the Sahara to India diverges, showing increasing top-of-atmosphere radiative forcing from shifting circulation and cloud patterns (S7 Figc, e; S8 Figa). Hydroclimate responses to eruptions are spatially heterogeneous, with weakened equatorial precipitation systems and strengthening over the southern Indian Ocean and North Atlantic, suggesting dynamic and thermodynamic adjustments (S1 Text).

Fig 1. Volcanic-induced temperature variability relative to unforced internal variability. (a) Median values (lines) and 95 %-confidence intervals (shading) for ensembles of ESM-modeled (pink) and emulated (red) global mean annual surface temperature (GMSAT) compared to the unforced variability component (blue). The emulated ensemble yields stable uncertainty estimates. (b) Additional SAT variability affects much of the world population, who are exposed to increasing uncertainty due to additional regional surface air temperature variability (relative to unforced variability). (c) Many IPCC regions [27], particularly in low-to mid-latitudes where inter-quartile ranges (IQR) of unforced surface air temperature variability are comparably low (left bars), experience a high relative increase of temperature variability through sporadic volcanic events (*, right bars).

Vegetation productivity anomalies and net carbon uptake relate to soil-moisture anomalies and are spatially confined (S8 Figb, c; S7 Figf). Following eruptions, equatorial Africa's vegetation productivity decreases due to changes in radiative and climatic drivers, but net carbon uptake into natural sinks increases locally. This is due to simulated slowing of soil organic matter decomposition under cooler, less humid conditions. In mid-latitudes (southern Africa, North America, parts of Eurasia), by contrast, intermittent volcanic forcing reduces natural carbon uptake. Here, precipitation surplus stimulates organic matter decomposition, which is not outweighed by increasing vegetation productivity (S8 Figc).

Climatological variables (precipitation, temperature, soil moisture) exhibit strong multi-annual to decadal variability increases under volcanic forcing (S7 Fig). The variability increase of GPP fluxes and net carbon uptake is lower but still substantial (ensemble spread +49 % for GPP; 35 % for net carbon uptake). This effect scales with

the aerosol load released within the averaging period. Differences in power spectral density are smaller for carbon flux than abiotic variables (S7 Figb, S9 Fig). On multi-annual timescales, net carbon uptake into natural sinks is slightly lower and, over 15–20 years, more variable in the forced ensemble. Significant spectral density differences persist for 11–18- and 23–28-year timescales in the global GPP flux.

Increasingly uncertain regional temperature pathways

Volcanic forcing increases multi-annual to multi-decadal temperature variability in future environmental and climatological projections. Consequently, uncertainty in the temperature pathway, which depends on the forcing's realization, increases. Across our 300-member ensemble, aerosol forcing increases the global mean temperature pathway's uncertainty envelope by a time-average of 0.32 K versus internal variability drawing on the emulation (Fig. 1a). The eight-member ESM ensemble shows an 0.20 K increase in average uncertainty, indicating an 89 % uncertainty growth in the global temperature pathway for the 300-member ensemble and 56 % for the simulation ensemble (Fig. 1c, legend). Simulated and emulated results suggest consistent regional heterogeneity in surface air temperature variability increases (Fig. 1). Consequently, under realistic volcanic forcing, around half the world population faces a 50 %+ increase in expected regional mean annual surface air temperature variability (Fig. 1b), mainly due to increased variability in eastern, southeastern, and central Asia.

Subtropical regions and mid-latitudes witness the highest relative increases over land and oceans (Fig. 1c). However, absolute uncertainties are about an order of magnitude smaller over oceans than on continents because the land-sea contrast in thermodynamic inertia causes lower unforced variability over waters. Intermittent aerosol forcing most strongly impacts regional temperature uncertainty relative to the unforced variability in a region spanning from northern Africa and the Mediterranean through central Eurasia to eastern Asia (Fig. 1c). In these regions, relative uncertainty rises between 68 % to 99 %, matching the near doubling globally. This trend is also evident in northern-central America (95 % relative increase), southeastern South America (78 %), and over the oceans (42 % – 119 %), excluding the Equatorial Pacific and Polar Oceans. In polar regions, South America and much of the northern hemisphere, internal climate variability is high, with volcanic forcing adding further minor uncertainty. Where internal climate variability is lower but substantial (e.g., in central North America, South Africa, northern Australia), volcanic-induced forced variability almost doubles it.

Heightened uncertainty in regional and global carbon fluxes with consequences for climate stabilization and net-zero pathways

We propagate the additional variability due to expected intermittent volcanic forcing using high correlations between climatic drivers and carbon flux responses (Fig. 2a-c, e) using a conservative, shared variance approach, which combines regional correlations with two levels of driver and response variables (Data and methods). Volcanic impacts start out with radiative imbalance as external forcing. This correlates mostly positively with surface air temperature (Fig. 2a). By first order, surface air temperature, emulated as the forced response to the radiative forcing from volcanic events, drives precipitation (Fig. 2b) and natural carbon fluxes (Fig. 2c, S10 Fig). Outside high-latitudes and eastern Asia, regional temperature–precipitation correlations are negative over land due to evapotranspiration feedbacks [28, 29]. Over oceans, volcanic-induced temperature and precipitation changes correlate positively, since temperature controls evaporation [29]. Equatorial Atlantic is an exception, showing a negative correlation due to its ties to neighboring landmasses. Surface air temperature inversely correlates with GPP in virtually the same regions (Fig. 2c), whereas precipitation correlates positively with

GPP, coinciding with a dominant moisture control on vegetation (Fig. 2e). Strong temperature control accompanies positive temperature–GPP correlations (e.g., in the northern hemisphere's mid- to high-latitudes, eastern Asia, North America's eastern coast, southwestern and southern South America, New Zealand), so precipitation weakly or inversely correlates with GPP here. Generally, GPP reponses depend more directly on soil moisture than precipitation. Considering soil moisture as a climatic driver strengthens the anti-correlation with GPP in high—latitudes, but yields similar shared variances elsewhere (Fig. S11 Fig).

Fig 2. Shared variances between climatic drivers and GPP, and the resulting supplementary GPP uncertainty from intermittent volcanic forcing in all IPCC regions. (a–c, e) Driver–response correlations of regional mean time series averaged over the simulation ensemble with long-term trends removed. To propagate supplementary uncertainty of intermittent aerosol forcing up to GPP, the first-order temperature response to external radiative forcing is explicitly emulated. Second- and third-order responses are estimated with the shared variance approach (Data and methods). (d) Increase in the 2.5–to–97.5 % inter-quartile range of regional GPP fluxes relative to spread from internal variability.

By propagating the additional variability of the regional temperature pathway through pair-wise regional correlations (Data and methods), we obtain increased uncertainties of regional GPP fluxes (Fig. 2d) and net uptake (S10 Fig). Substantial GPP uncertainty increases are comparably localized, particularly in subtropical and some temperate regions, most notably in eastern Asia (25 % relative to internal), northern Central America (26 %), and northern and central Australia (22 % to 40 %). Relative uncertainty rises by 15 % in northern South America, 15 % in southern Asia, 18 %–21 % in southern Africa, and 13 % in the Mediterranean. While the shared variance approach suggests GPP flux uncertainty increases substantially, it remains small compared to total regional GPP turnover (S12 Fig).

The propagated uncertainty increase of net carbon uptake is substantial when compared to the total annual uptake particularly over land (S12 Fig). Across low and mid-latitude regions, it reaches a 35 % median, due to high variability in regional carbon sinks relative to net carbon uptake. We also obtain uncertainty estimates for oceans. Since CO_2 water-solubility is temperature-dependent, the pattern and magnitude of the oceanic impacts follow regional temperature uncertainty (S10 Fig, +2–17 % over some non-polar oceans). Despite their varying influence on total annual flux rates, the spatial patterns and magnitude of propagated uncertainty relative to the internal component align closely with the GPP flux (median of land regions 5.7 %, maximum 34 %; Fig. 2, S10 Fig).

The additional variability impact from climatic drivers on the carbon cycle response is timescale dependent (Fig. 3). Concerning climatic drivers, the variance increases prominently by up to 114 % in global mean surface air temperature on forcing-dominated timescales, with a large ensemble spread of 69 %–165 % (95 % range). The propagated variance increase for global precipitation is similar but muted, peaking at an 87 % variability increase (50 %–128 %). This muting is expected given the share of precipitation variability not temperature correlated. Notably, muting is more pronounced on multi-annual to decadal timescales than for multi-decadal variability modes. Differing covariance characteristics between vegetation productivity, net carbon uptake, and the two climatic driver variables considered here (Fig. 2, S10 Fig) lead to differences between vegetation productivity and net carbon uptake. The maximum variance increase is 42 % (25–60 %) at 10–20 year timescales, while vegetation productivity shows 47 % (20 %–78 %) across 20–30 years (Fig. 3).

Variability in the Earth system from intermittent volcanic forcing increases SSP

Fig 3. Time-scale dependence of global variance increase from intermittent volcanic forcing for mean surface air temperature, annual precipitation, GPP flux, and net natural carbon uptake. Values are relative to internal variability. Temperature variance increase is directly emulated, while precipitation, GPP and natural carbon flux are inferred indirectly (Data and methods). Thick lines mark the ensemble mean; shading and thin lines indicate the 95 %-confidence range.

storyline uncertainty (Fig. 4). Notably, stabilizing global climate and achieving net-zero emissions can be delayed or accelerated (Fig. 4a, d). A wider uncertainty envelope implies a higher probability that a single realization will deviate farther from the ensemble mean pathway. Global mean surface air temperature and global precipitation show predominantly negative excursions arising from the cooling effect of stratospheric aerosols and the Clausius–Clapeyron relationship. This asymmetry makes it more likely to exceed global warming targets later when volcanic eruptions occur (Fig. 4a). Equally, a realization is more likely to temporarily reach or undercut a global warming target early in stabilization or after overshooting it (Fig. 4, Fig. 4a). However, volcanic events are sporadic, so realizations do not always follow a cool pathway even if they reach comparably cool temperatures or high natural carbon uptake.

Fig 4. Increased variability along future global climate and carbon cycle pathways from volcanic forcing. (a) Mean surface air temperature anomaly, (b) mean precipitation, (c) annual GPP flux, (d) net annual carbon uptake into terrestrial and marine sinks for 50-member MPI-ESM ensembles of the SSPs 1-2.6, 2-4.5, and 5-8.5 [25] as indicated. Solid lines represent the ensemble mean. Shading indicates the 95 % ensemble spread without volcanic forcing (no VF, colored) and with intermittent volcanic forcing (IVF, gray). Estimates of increased uncertainty employ the shared variance approach (Data and methods) corrected for slight differences between the internal variability of the 50-member ensembles and that diagnosed by the emulator for the explicitly forced IVF ensemble. Markers in (a) indicate the raised likelihood for a delayed surpassing of a global warming target. In (d), they illustrate the increased likelihood of more effective (5-8.5) and less effective natural carbon sinks (1-2.6).

Owing to spatially varied hydrological cycle responses to global cooling, additional variability in the global GPP pathway and net uptake is not unidirectional (Fig. 4c). Considering intermittent volcanic forcing increases the likelihood that natural carbon sinks, which buffer anthropogenic emissions, will vary more strongly in effectiveness (Fig. 4d). Intermittent volcanic forcing can both delay and advance achieving global net-zero emissions by modulating natural carbon sink efficacy.

Discussion

Marine and terrestrial carbon sinks buffer a substantial share of CO_2 emissions in future climate pathways. For many mid- and low-latitude regions, our results suggest intermittent volcanic forcing increases net carbon uptake uncertainty on land by 35 %+ relative to net annual uptake averaged over the scenario's CO_2 rise and peak phases where uptake is highest (S7 Fig). Globally, we find a 34 % increase in the uncertainty envelope using a conservative estimation technique that aggregates only the uncertainty increase explained linearly through covariance. Volcanic eruptions could both advance and delay reaching net-zero carbon emissions by altering natural carbon sink efficacy [30]. These sinks are pivotal in climate stabilization scenarios, with increased uncertainty impacting net-zero or net-negative emissions planning and limiting

planetary temperature rise. Accounting for and communicating net-zero's lower temporal certainty in state–of–the–art climate projections is crucial for avoiding misconceptions about knowns and unknowns regarding CO_2-driven climate change.

Carbon flux uncertainty originates from increased temperature and hydroclimate variability. Our global temperature uncertainty increase estimate (0.32 K, 89 % of the internal component) is comparable to estimates by Chim et al. (2025) [2] (0.3 K, 100 %) but exceeds Bethke et al. (2017) [1] (0.2 K, 50 %). The differences stem from MPI-ESM's higher climate sensitivity than the NorESM model [31] employed by Bethke et al. (2017) [1]. Our study accounts for under sampling of smaller volcanic events in ice-core records (Data and methods). The smaller 60-member ensemble in Bethke et al. (2017) [1] could cause a negative bias of 0.02 to 0.05 K (S6 Fig). Our results suggest that ensemble sizes of 150+ members ensure convergence and time-stable uncertainty estimates (S2 Text, Fig. S6 Fig).

Our results reveal substantial spatial heterogeneity. Annual mean surface air temperature uncertainty increases of at least 50 % affect half the global population [32], particularly across Asia, Central America, Africa, and Australia. Contributing factors likely include the many active volcanoes near the equator, modulating circulation patterns, and land–sea contrasts after outbreaks. Given the links between mean temperature, temperature and hydroclimate variability, and weather extremes, future research should explore how increased regional uncertainty affects the probability of severe extremes and how societies should adapt. Uncertainty increases at or well above 35 % of net (terrestrial) carbon uptake, especially in subtropical regions, suggest hydroclimate shifts after volcanic events increase carbon flux uncertainty. The subtropics substantially contribute to the land carbon sinks and play a key role in shaping its variability [33].

Our ESM emulator can reproduce internal and forced variability consistent with MPI-ESM's response to varying aerosol forcing, presenting an optimized complexity design between large, comprehensive simulation ensembles with intermittent aerosol forcing, and standard ScenarioMIP projections with constant mean aerosol forcing envisaged in CMIP7 [6]. Fitting and inverting the emulator requires fewer computational resources than running the full-scale model repeatedly and reliably reproduces key spatial and temporal characteristics. We utilized eight 185-year explicit ESM simulations to estimate the emulator's parameters, which vary only slightly (S4 Fig). Meanwhile, the underlying inference algorithm performs well even for a single, sufficiently long, realization [15]. We expect this will enable the inferring of statistically stable multi-model uncertainty envelopes from a single to few stochastically forced, multi-event runs per model, not limited to, but ideally with interactive stratospheric aerosols [34].

We propagate regional uncertainties from climatic drivers via shared variances into carbon fluxes. Emulating spatiotemporal carbon fluxes directly requires adjusting our emulator since Schillinger et al. (2022) [15]'s algorithm assumes Gaussian-distributed variables. Our emulator uses truncated Empirical Orthogonal Functions (Data and methods), which omit some polar-region variability. This could be reduced by increasing the traceable orthogonal modes or exploring other dimensionality reduction approaches. Our approach adapts seamlessly to model improvements and various model setups, scenarios, or forcing datasets. This makes it ideal for augmenting diverse, multi-source datasets with an uncertainty envelope from sporadic volcanic forcing with low effort.

We assume future eruptions occur with similar frequency as in the past. Magnitudes and timings of past eruptions as analogues for future events can only be approximate. Eruption frequency and their climate impact could change under warming due to isostatic adjustments from ice sheet melt, more frequent heavy precipitation, sea level rise, and circulation changes [35, 36]. Expanding the paleo record and employing it to

improve ESM accuracy [35] could improve the model representation of state- and pathway-dependent dynamics. Our approach can adapt to improvements that alter climate sensitivity by adjusting the box model's response parameters (Data and methods). It could also identify state-dependent sensitivities of (paleo-)data and models [3], and differentiate between consequences for internal climate variability and forced response.

Our estimates of supplementary future natural carbon uptake variability could be influenced by inaccurately represented carbon flux dynamics and biosphere–climate interactions in our emulator and the underlying MPI-ESM. Over the historical period, global variability of net uptake and GPP flux in MPI-ESM corresponds with the global carbon budget [37]. Yet over the last few thousand years, MPI-ESM, like most ESMs, displays less regional variability than reconstructions [38]. Our sensitivity experiments explored whether (negative) vapor and (positive) sensible heat feedback could increase multi-annual and multi-decadal internal temperature variability components without changing the forced response to volcanic events (S3 Text, S16 Fig). Too low internal variability of surface temperature and terrestrial carbon fluxes could shift the increased uncertainty envelope's relative importance. The vegetation model tends to underestimate the compounding multi-annual to decadal effects of consecutive volcanic events on the moisture budget (S2 Text), possibly leading to a low bias in vegetation productivity and soil respiration responses. These effects are unlikely to qualitatively alter the Earth system's response to intermittent aerosol forcing but highlight limitations of ESMs in capturing variability. Future research could therefore explore how varying parametrizations of surface–atmosphere interactions affects climate stability and the Earth system's forced response to sporadic volcanic aerosol emissions.

In conclusion, we determined the supplementary uncertainty in global and regional surface climate and carbon fluxes resulting from realistically varying volcanic aerosol concentrations during a temperature overshoot. In our ensemble, intermittent forcing increased global mean annual temperature uncertainty by 89 % relative to internal variability, and we inferred a 34 % uncertainty rise in global annual carbon uptake into natural sinks. This implies achieving net-zero CO_2 emissions and the 2 °C target can be delayed or accelerated through stratospheric aerosol forcing, underscoring its necessary inclusion in climate stabilization pathway estimates. Our scaling factors provide a first-order estimate of supplementary uncertainty due to intermittent aerosol forcing for any projection pathway or model configuration. We suggest operationalizing such emulators to enhance future climate assessments encompassing forced responses to volcanic eruptions, or for exploring geoengineering pathways relying on stratospheric aerosol injections.

Supporting information

S1 Text Climatic responses to volcanic forcing.

S2 Text Probing the sensitivity of uncertainty estimates on ensemble size and forcing characteristics.

S3 Text Destabilizing land–atmosphere feedbacks enhance internal temperature variability without affecting the forced response.

S1 Table ClimBayes prior ranges for EBM fitting.

S1 Fig. Forward and inverse application of the spatiotemporal emulator.

S2 Fig. Spatial modes obtained from EOFs.

S3 Fig. Exemplary fits of the EBM to principal components.

S4 Fig. Exemplary EBM parameters obtained for the principal components.

S5 Fig. Sensitivity testing of the predicted temperature uncertainty.

S6 Fig. Convergence of temperature uncertainty estimates.

S7 Fig. Global and regional effects of intermittent volcanic forcing.

S8 Fig. Additional regional climatologies.

S9 Fig. Global mean power spectral density for all simulations.

S10 Fig. Shared variances between climatic drivers and f_{nat}, with resulting supplementary regional uncertainty.

S11 Fig. Shared variances between temperature and soil moisture as climatic drivers and f_{GPP} in response, with resulting supplementary regional uncertainty.

S12 Fig. Absolute and relative regional f_{GPP} and f_{nat} uncertainty increase.

S13 Fig. Widened uncertainty distributions due to varying volcanic forcing.

S14 Fig. Climatological anomalies of the sensitivity experiments with lowered C4 albedo.

S15 Fig. Climatological anomalies of the sensitivity experiments with disabled climate change feedback on vegetation.

S16 Fig. Effect of vegetation feedbacks on climate's internal variability and forced response.

S17 Fig. Effect of vegetation feedbacks on the internal variability of global mean surface air temperature, f_{GPP}, and f_{nat}.

Acknowledgments

The authors acknowledge the German Climate Computing Centre (DKRZ) for providing resources and compute time through the CITRONE and EXPLAINSTATES projects, granted through the DKRZs Scientific Steering Committee (WLA). We thank all contributors to the Max Planck Institute for Meteorology Earth system model for making their code available and accessible, and Hazel Rowland for assistance in editing the original draft.

References

1. Bethke I, Outten S, Otterå OH, Hawkins E, Wagner S, Sigl M, et al. Potential volcanic impacts on future climate variability. Nature Climate Change. 2017;7(11):799-805. doi:10.1038/nclimate3394.

2. Chim MM, Aubry TJ, Smith C, Schmidt A. Neglecting future sporadic volcanic eruptions underestimates climate uncertainty. Communications Earth & Environment. 2025;6(1):236. doi:10.1038/s43247-025-02208-1.

3. Ellerhoff B, Kirschner MJ, Ziegler E, Holloway MD, Sime L, Rehfeld K. Contrasting State-Dependent Effects of Natural Forcing on Global and Local Climate Variability. Geophysical Research Letters. 2022;49(10). doi:10.1029/2022gl098335.

4. Pausata FSR, Chafik L, Caballero R, Battisti DS. Impacts of high-latitude volcanic eruptions on ENSO and AMOC. Proceedings of the National Academy of Sciences. 2015;112(45):13784-8. doi:10.1073/pnas.1509153112.

5. Schindlbeck-Belo JC, Toohey M, Jegen M, Kutterolf S, Rehfeld K. PalVol v1: a proxy-based semi-stochastic ensemble reconstruction of volcanic stratospheric sulfur injection for the last glacial cycle (140 000–50 BP). Earth System Science Data. 2023;16(2):1063-81. doi:10.5194/essd-16-1063-2024.

6. Aubry TJ, Toohey M, Khanal S, Chim MM, Verkerk M, Johnson B, et al. Stratospheric aerosol forcing for CMIP7 (part 1): Optical properties for pre-industrial, historical, and scenario simulations (version 2.2.1). EGUsphere. 2025;2025:1-53. doi:10.5194/egusphere-2025-4990.

7. Koven CD, Arora VK, Cadule P, Fisher RA, Jones CD, Lawrence DM, et al. Multi-century dynamics of the climate and carbon cycle under both high and net negative emissions scenarios. Earth System Dynamics. 2022;13(2):885-909. See notes for preprint. doi:10.5194/esd-13-885-2022.

8. Calvin K, Dasgupta D, Krinner G, Mukherji A, Thorne PW, Trisos C, et al. IPCC, 2023: Climate Change 2023: Synthesis Report. Contribution of Working Groups I, II and III to the Sixth Assessment Report of the Intergovernmental Panel on Climate Change [Core Writing Team, H. Lee and J. Romero (eds.)]. IPCC, Geneva, Switzerland. Geneva, Switzerland: IPCC; 2023. doi:10.59327/ipcc/ar6-9789291691647.

9. Melnikova I, Boucher O, Cadule P, Ciais P, Gasser T, Quilcaille Y, et al. Carbon Cycle Response to Temperature Overshoot Beyond 2°C: An Analysis of CMIP6 Models. Earth's Future. 2021;9(5):1-19. Overshoot scenario response of CMIP6 subset. doi:10.1029/2020ef001967.

10. DeVries T. The Ocean Carbon Cycle. Annual Review of Environment and Resources. 2022;47(1):317-41. doi:10.1146/annurev-environ-120920-111307.

11. Gentine P, Green JK, Guérin M, Humphrey V, Seneviratne SI, Zhang Y, et al. Coupling between the terrestrial carbon and water cycles—a review. Environmental Research Letters. 2019;14(8):083003. doi:10.1088/1748-9326/ab22d6.

12. Prescott CE. Litter decomposition: what controls it and how can we alter it to sequester more carbon in forest soils? Biogeochemistry. 2010;101(1-3):133-49. doi:10.1007/s10533-010-9439-0.

13. Green JK, Seneviratne SI, Berg AM, Findell KL, Hagemann S, Lawrence DM, et al. Large influence of soil moisture on long-term terrestrial carbon uptake. Nature. 2019;565(7740):476-9. doi:10.1038/s41586-018-0848-x.

14. Riahi K, Vuuren DPv, Kriegler E, Edmonds J, O"Neill BC, Fujimori S, et al. The Shared Socioeconomic Pathways and their energy, land use, and greenhouse gas emissions implications: An overview. Global Environmental Change. 2017;42:153-68. SSP baselines reference. doi:10.1016/j.gloenvcha.2016.05.009.

15. Schillinger M, Ellerhoff B, Scheichl R, Rehfeld K. Separating internal and externally forced contributions to global temperature variability using a Bayesian stochastic energy balance framework. Chaos: An Interdisciplinary Journal of Nonlinear Science. 2022;32(11):113146. arXiv:2206.14573. doi:10.1063/5.0106123.

16. Verkerk M, Aubry TJ, Smith C, Hopcroft PO, Sigl M, Tierney JE, et al. Using reduced-complexity volcanic aerosol and climate models to produce large ensemble simulations of Holocene temperature. Climate of the Past. 2025;21(10):1755-78. doi:10.5194/cp-21-1755-2025.

17. Lütjens B, Ferrari R, Watson-Parris D, Selin NE. The Impact of Internal Variability on Benchmarking Deep Learning Climate Emulators. Journal of Advances in Modeling Earth Systems. 2025;17(8). doi:10.1029/2024ms004619.

18. Mauritsen T, Bader J, Becker T, Behrens J, Bittner M, Brokopf R, et al. Developments in the MPI-M Earth System Model version 1.2 (MPI-ESM1.2) and Its Response to Increasing CO2. Journal of Advances in Modeling Earth Systems. 2019;11(4):998-1038. MPI-ESM1.2 + CO2 response Most important: 5. Revisions to HAMOCC6 6. Revisions to JSBACH. doi:10.1029/2018ms001400.

19. Meinshausen M, Nicholls ZRJ, Lewis J, Gidden MJ, Vogel E, Freund M, et al. The shared socio-economic pathway (SSP) greenhouse gas concentrations and their extensions to 2500. Geoscientific Model Development. 2020;13(8):3571-605. - long term GHG conc extensions - discusses underlying assumptions on emission (and CDR) pathway extensions. doi:10.5194/gmd-13-3571-2020.

20. Stevens B, Giorgetta M, Esch M, Mauritsen T, Crueger T, Rast S, et al. Atmospheric component of the MPI-M Earth System Model: ECHAM6. Journal of Advances in Modeling Earth Systems. 2013;5(2):146-72. doi:10.1002/jame.20015.

21. Jungclaus JH, Keenlyside N, Botzet M, Haak H, Luo JJ, Latif M, et al. Ocean Circulation and Tropical Variability in the Coupled Model ECHAM5/MPI-OM. Journal of Climate. 2006;19(16):3952-72. doi:10.1175/jcli3827.1.

22. O'Neill BC, Tebaldi C, Vuuren DPv, Eyring V, Friedlingstein P, Hurtt G, et al. The Scenario Model Intercomparison Project (ScenarioMIP) for CMIP6. Geoscientific Model Development. 2016;9(9):3461-82. Reference for ScenarioMIP (concentration-driven). doi:10.5194/gmd-9-3461-2016.

23. Toohey M, Stevens B, Schmidt H, Timmreck C. Easy Volcanic Aerosol (EVA v1.0): an idealized forcing generator for climate simulations. Geoscientific Model Development. 2016;9(11):4049-70. doi:10.5194/gmd-9-4049-2016.

24. Storch HV, Navarra A. Analysis of climate variability: applications of statistical techniques. Springer Science & Business Media;.

25. Olonscheck D, Suarez-Gutierrez L, Milinski S, Beobide-Arsuaga G, Baehr J, Fröb F, et al. The New Max Planck Institute Grand Ensemble With CMIP6 Forcing and High-Frequency Model Output. Journal of Advances in Modeling Earth Systems. 2023;15(10). doi:10.1029/2023ms003790.

26. Ellerhoff B, Rehfeld K. Probing the timescale dependency of local and global variations in surface air temperature from climate simulations and reconstructions of the last millennia. Physical Review E. 2021;104(6):064136. arXiv:2102.00458. doi:10.1103/physreve.104.064136.

27. Iturbide M, Gutiérrez JM, Alves LM, Bedia J, Cerezo-Mota R, Cimadevilla E, et al. An update of IPCC climate reference regions for subcontinental analysis of climate model data: definition and aggregated datasets. Earth System Science Data. 2020;12(4):2959-70. doi:10.5194/essd-12-2959-2020.

28. Berg A, Lintner BR, Findell K, Seneviratne SI, Hurk Bvd, Ducharne A, et al. Interannual Coupling between Summertime Surface Temperature and Precipitation over Land: Processes and Implications for Climate Change. Journal of Climate. 2015;28(3):1308-28. doi:10.1175/jcli-d-14-00324.1.

29. Adler RF, Gu G, Wang J, Huffman GJ, Curtis S, Bolvin D. Relationships between global precipitation and surface temperature on interannual and longer timescales (1979–2006). Journal of Geophysical Research: Atmospheres. 2008;113(D22). doi:10.1029/2008jd010536.

30. Zhang X, Peng S, Ciais P, Wang Y, Silver JD, Piao S, et al. Greenhouse Gas Concentration and Volcanic Eruptions Controlled the Variability of Terrestrial Carbon Uptake Over the Last Millennium. Journal of Advances in Modeling Earth Systems. 2019;11(6):1715-34. doi:10.1029/2018ms001566.

31. Bock L, Lauer A. Cloud properties and their projected changes in CMIP models with low to high climate sensitivity. Atmospheric Chemistry and Physics. 2023;24(3):1587-605. doi:10.5194/acp-24-1587-2024.

32. Tatem AJ. WorldPop, open data for spatial demography. Scientific Data. 2017;4(1):170004. doi:10.1038/sdata.2017.4.

33. Ahlström A, Raupach MR, Schurgers G, Smith B, Arneth A, Jung M, et al. The dominant role of semi-arid ecosystems in the trend and variability of the land CO2 sink. Science. 2015;348(6237):895-9. doi:10.1126/science.aaa1668.

34. Timmreck C, Mann GW, Aquila V, Hommel R, Lee LA, Schmidt A, et al. The Interactive Stratospheric Aerosol Model Intercomparison Project (ISA-MIP): motivation and experimental design. Geoscientific Model Development. 2018;11(7):2581-608. doi:10.5194/gmd-11-2581-2018.

35. Aubry TJ, Farquharson JI, Rowell CR, Watt SFL, Pinel V, Beckett F, et al. Impact of climate change on volcanic processes: current understanding and future challenges. Bulletin of Volcanology. 2022;84(6):58. doi:10.1007/s00445-022-01562-8.

36. Huybers P, Langmuir C. Feedback between deglaciation, volcanism, and atmospheric CO2. Earth and Planetary Science Letters. 2009;286(3-4):479-91. doi:10.1016/j.epsl.2009.07.014.

37. Friedlingstein P, O'Sullivan M, Jones MW, Andrew RM, Hauck J, Landschützer P, et al. Global Carbon Budget 2024. Earth System Science Data. 2025;17(3):965-1039. doi:10.5194/essd-17-965-2025.

38. Laepple T, Ziegler E, Weitzel N, Hébert R, Ellerhoff B, Schoch P, et al. Regional but not global temperature variability underestimated by climate models at supradecadal timescales. Nature Geoscience. 2023;16(11):958-66. doi:10.1038/s41561-023-01299-9.

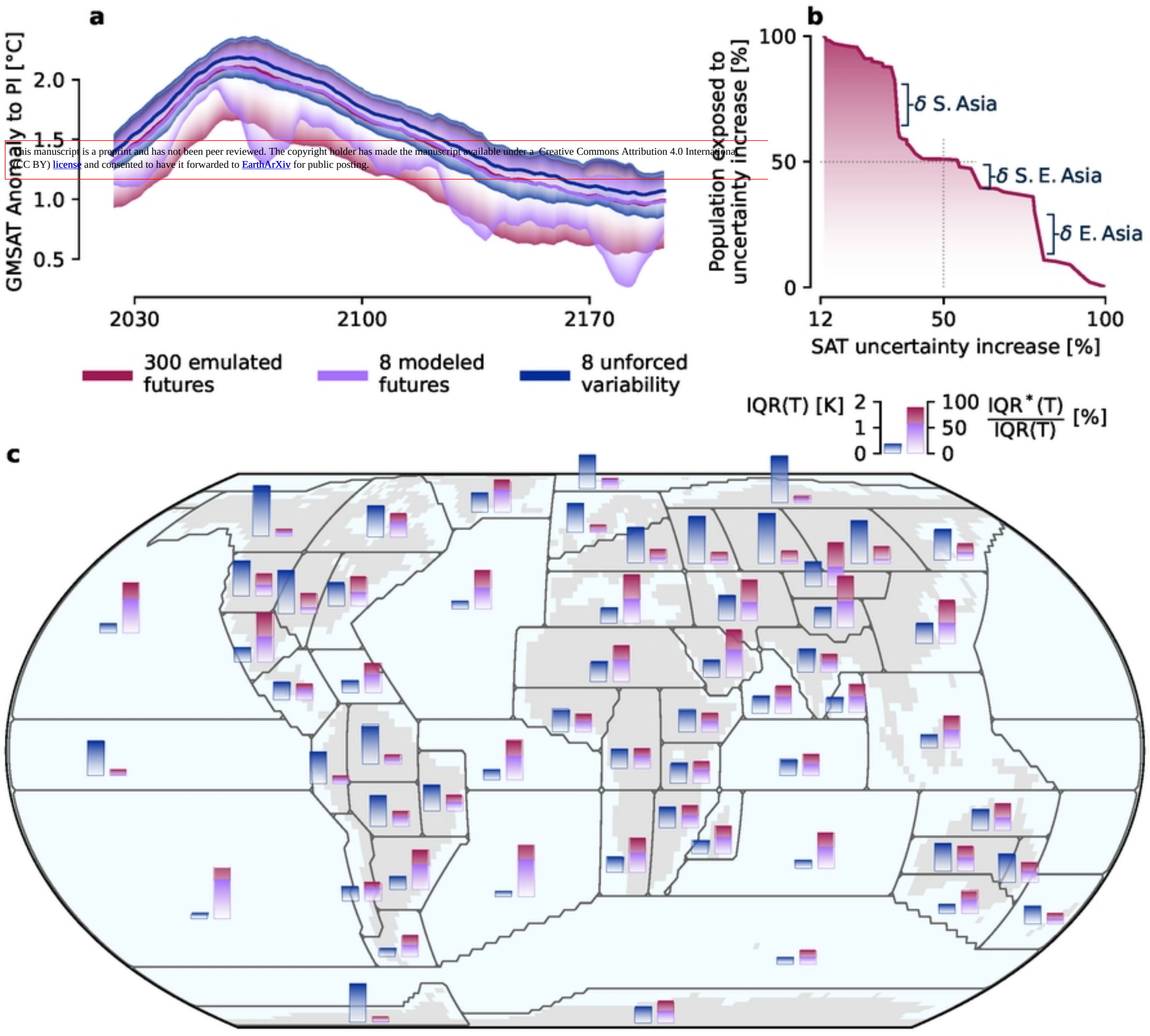

Figure 1

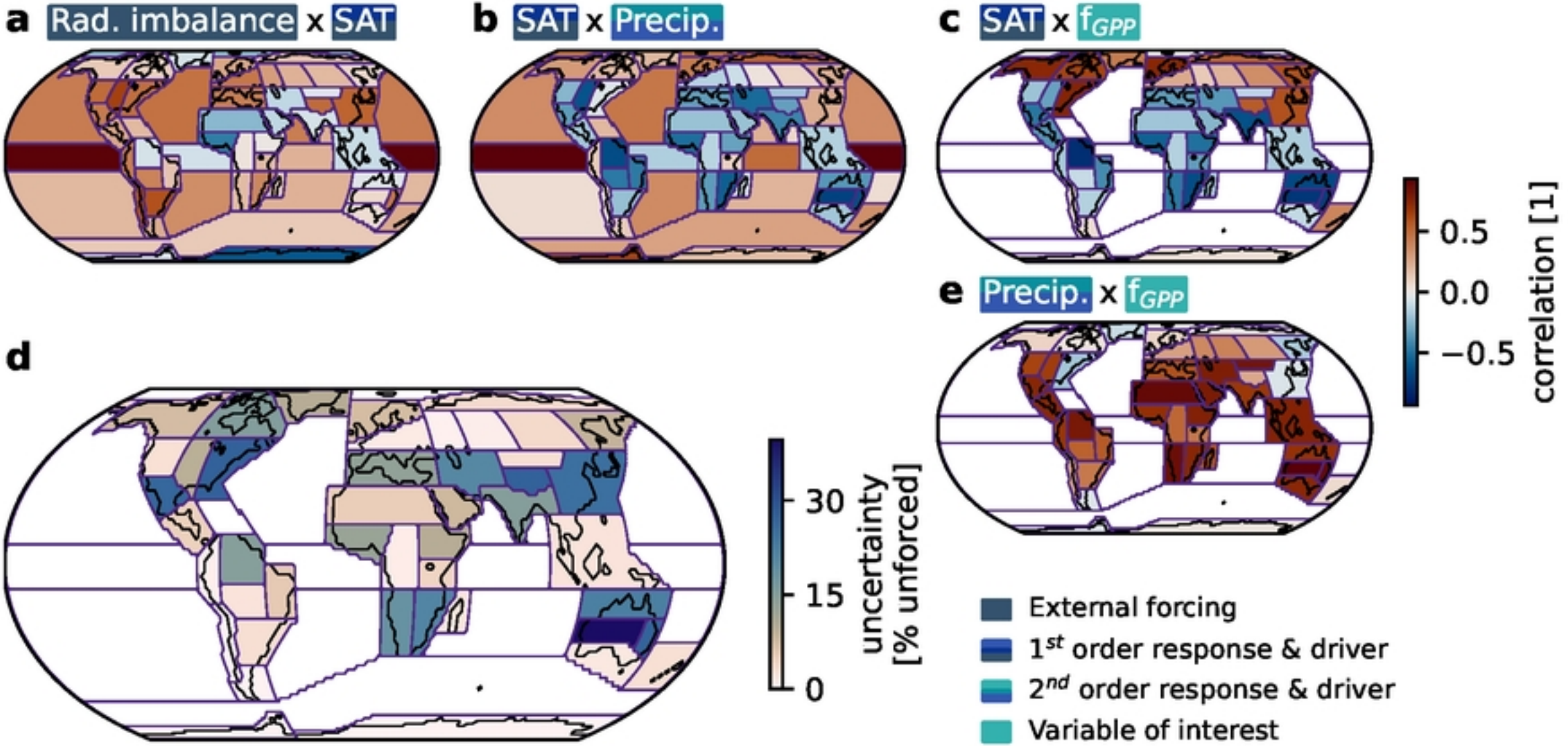
a Rad. imbalance x SAT
b SAT x Precip.
c SAT x f_{GPP}
e Precip. x f_{GPP}
d
0.5
0.0
−0.5
correlation [1]
30
15
0
uncertainty [% unforced]
External forcing
1st order response & driver
2nd order response & driver
Variable of interest

Figure 2

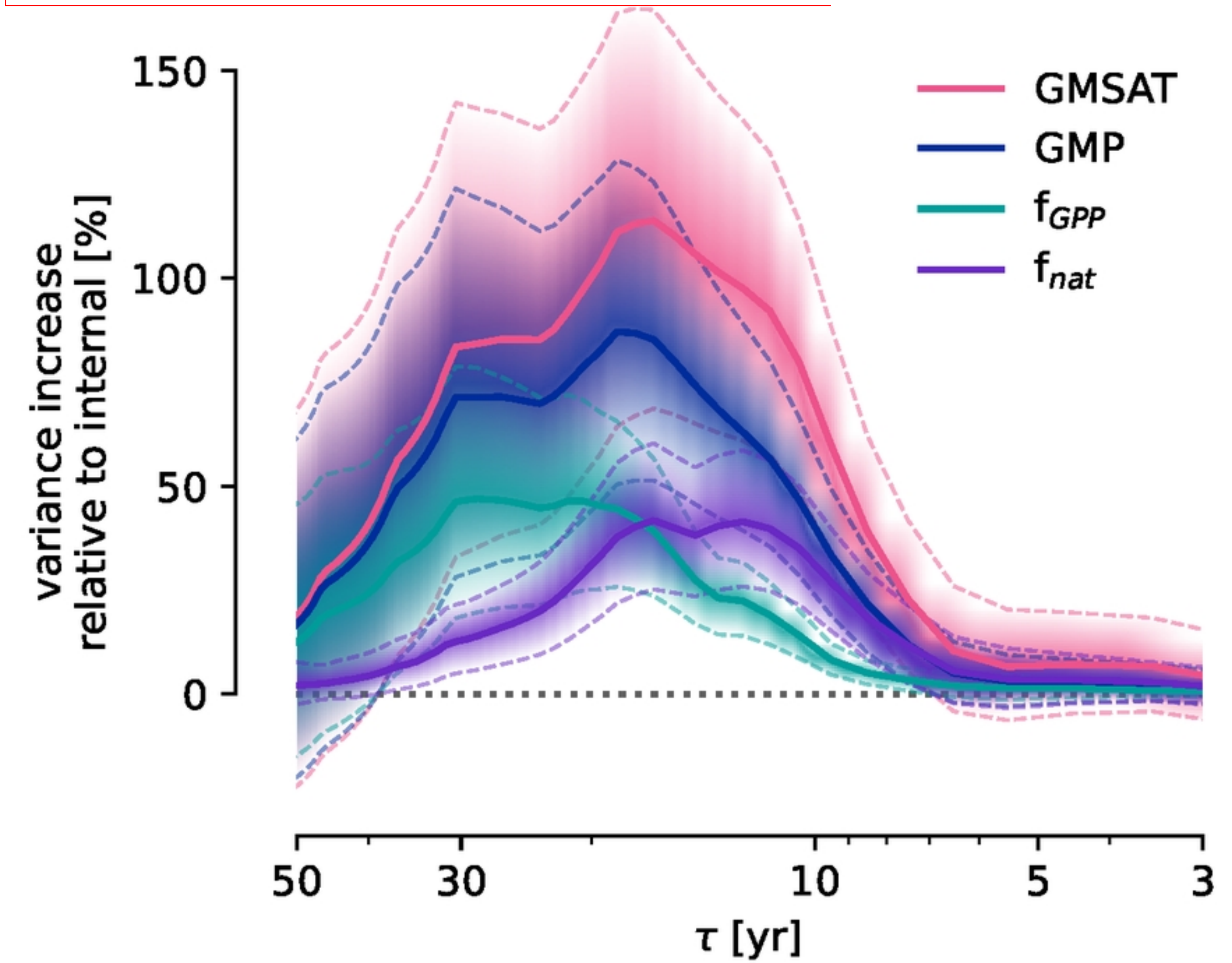

Figure 3

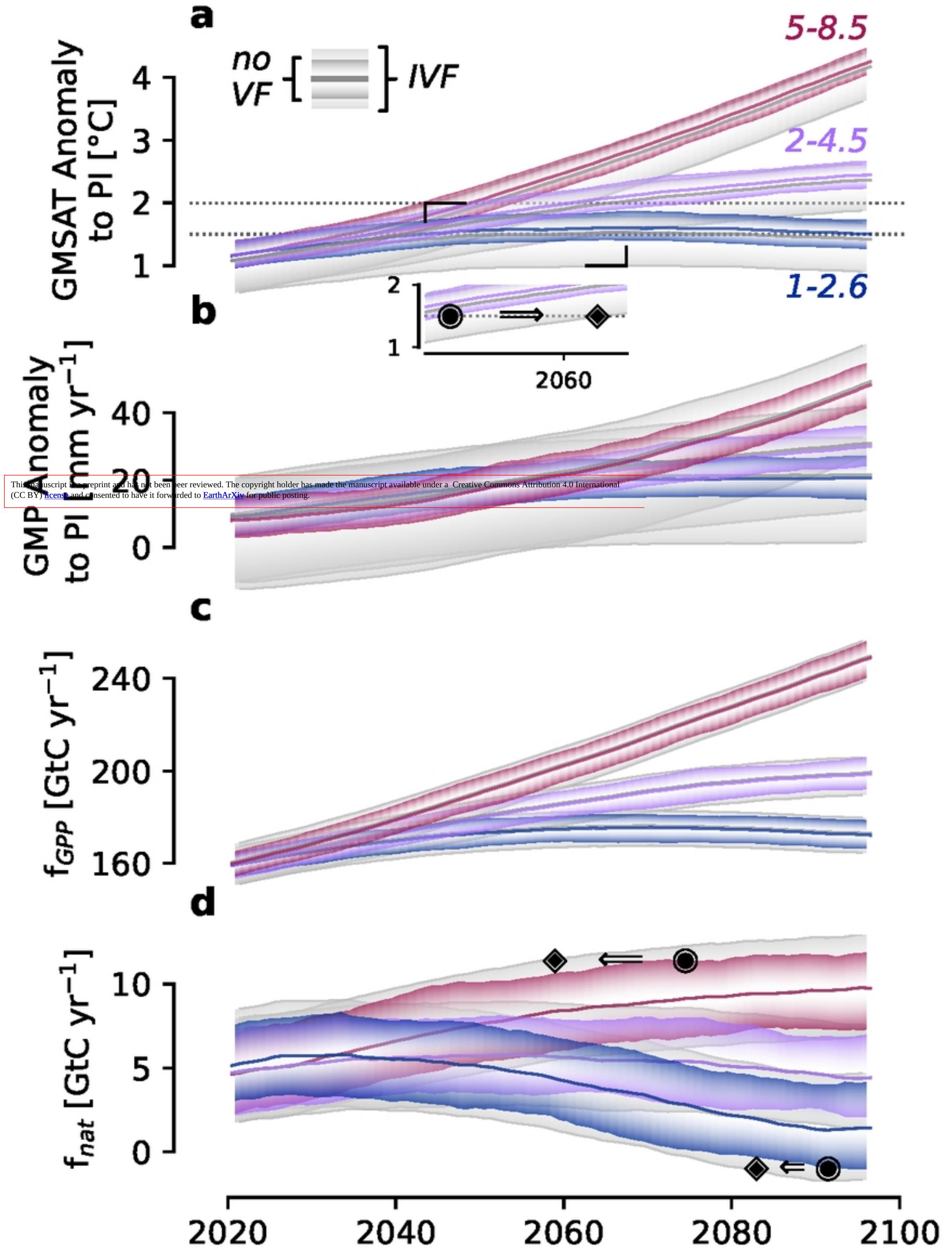

Figure 4